Biochemistry **2004,** *43,* 3772−3782

Crystal Structures of an Intrinsically Active Cholera Toxin Mutant Yield Insight into the Toxin Activation Mechanism[†,‡]

Claire J. O'Neal,[§] Edward I. Amaya,[∥,⊥] Michael G. Jobling,[∥] Randall K. Holmes,[∥] and Wim G. J. Hol*,[#]

Departments of Chemistry and Biochemistry, Biomolecular Structure Center, and Howard Hughes Medical Institute, University of Washington, Seattle, Washington 98195, and Department of Microbiology, University of Colorado Health Sciences Center, Denver, Colorado 80220

Received November 11, 2003; Revised Manuscript Received January 30, 2004

ABSTRACT: Cholera toxin (CT) is a heterohexameric bacterial protein toxin belonging to a larger family of A/B ADP-ribosylating toxins. Each of these toxins undergoes limited proteolysis and/or disulfide bond reduction to form the enzymatically active toxic fragment. Nicking and reduction render both CT and the closely related heat-labile enterotoxin from *Escherichia coli* (LT) unstable in solution, thus far preventing a full structural understanding of the conformational changes resulting from toxin activation. We present the first structural glimpse of an active CT in structures from three crystal forms of a single-site A-subunit CT variant, Y30S, which requires no activational modifications for full activity. We also redetermined the structure of the wild-type, proenzyme CT from two crystal forms, both of which exhibit (i) better geometry and (ii) a different A2 "tail" conformation than the previously determined structure [Zhang et al. (1995) *J. Mol. Biol. 251*, 563−573]. Differences between wild-type CT and active CTY30S are observed in A-subunit loop regions that had been previously implicated in activation by analysis of the structure of an LT A-subunit R7K variant [van den Akker et al. (1995) *Biochemistry 34*, 10996−11004]. The 25−36 activation loop is disordered in CTY30S, while the 47−56 active site loop displays varying degrees of order in the three CTY30S structures, suggesting that disorder in the activation loop predisposes the active site loop to a greater degree of flexibility than that found in unactivated wild-type CT. On the basis of these six new views of the CT holotoxin, we propose a model for how the activational modifications experienced by wild-type CT are communicated to the active site.

Cholera, caused by *Vibrio cholerae*, and traveler's and children's diarrhea, caused by enterotoxigenic *Escherichia coli* (ETEC), are responsible for tens of thousands of deaths per year in areas lacking proper water sanitation (*1*). The main virulence factors responsible for these diseases are heterohexameric AB_5 protein toxins, cholera toxin (CT),[1] and heat-labile enterotoxin (LT), respectively, which share over 80% sequence identity.

CT and LT belong to a larger family of ADP-ribosylating bacterial toxins that adopt an overall A/B subunit morphology. Well-studied members of this family include diphtheria toxin (DT), pertussis toxin (PT), and exotoxin A from *Pseudomonas aeruginosa* (PE). These toxins contain an enzyme component, A, and a nontoxic receptor-binding component, B, both of which are required for in vivo toxic activity (*2*−*5*). The toxic fragment of these A/B toxins catalyzes the transfer of ADP-ribose from NAD^+ to an acceptor residue in a eukaryotic target protein that differs among the toxins. CT and LT ADP-ribosylate Arg 201 of the α-subunit of the heterotrimeric G-signaling protein (G_S), thereby permanently activating the signal cascade pathway involving adenylate cyclase. The resulting elevation of cAMP causes a massive efflux of ions from intestinal epithelial cells, leading to dehydration and, in severe cases, death (*6*).

Initially, A/B bacterial toxins exist as proenzymes and must be modified by limited proteolysis and/or disulfide bond reduction for full function (*3*−*5*, *7*). In the case of CT and LT, these modifications divide the 240-residue A subunit into two functional parts: the enzymatic portion, A1 (residues 1−192 or −194), and A2 (residues 193− or 195−240), which tethers A1 to the receptor-binding pentamer of B-subunits (B_5). CT and LT A1 and A2 are initially covalently linked through their mutual peptide chain and a

---

[†] Funding for this work was provided by grants from the National Institutes of Health to W.G.J.H. (AI-34501) and to R.K.H. (AI-31940) and by a Howard Hughes Medical Institute predoctoral fellowship to C.J.O.

[‡] Coordinates and structure factors have been deposited in the Protein Data Bank with accession codes 1S5B (CTY30S form 3), 1S5C (CTY30S form 1), 1S5D (CTY30S form 2), 1S5E (wild-type CT form 1), and 1S5F (wild-type CT form 2).

* To whom correspondence should be addressed at the Biological Structure Center, University of Washington, Box 357742, Seattle, WA 98195. Telephone: (206) 685-7044. Fax: (206) 685-7002. E-mail: wghol@u.washington.edu.

[§] Department of Chemistry and Biomolecular Structure Center, University of Washington.

[∥] University of Colorado.

[⊥] Current address: MedImmune, Inc., Gaithersburg, MD 20878.

[#] Department of Biochemistry, Biomolecular Structure Center, and Howard Hughes Medical Institute, University of Washington.

[1] Abbreviations: CT, cholera toxin; LT, heat-labile enterotoxin; CTY30S, CT with an A1:Y30S substitution; DT, diphtheria toxin; PE, *Pseudomonas aeruginosa* exotoxin A; PT, pertussis toxin; NAD, β-nicotinamide adenine dinucleotide; ADP, adenosine diphosphate; RMSD, root mean square deviation; cAMP, cyclic adenosine monophosphate; ER, endoplasmic reticulum.

10.1021/bi0360152 CCC: $27.50

disulfide bond between Cys 187 and Cys 199; these linkages must both be severed for full enzymatic activity (*5*). Nicking of the polypeptide chain and reduction of the disulfide bond occur over 20 Å away from the proposed CT/LT active site, and the precise manner by which these changes are communicated to and result in a functional active site is still unknown. DT and PE undergo similar activational processes, which have not hindered the structural study of both proenzyme and activated forms of DT and PE (*8*, *9*). However, CT and LT crystal structures reported to date represent only inactive, proenzyme toxin forms (*10*, *11*). Attempts to obtain a crystal structure of activated CT or LT have been unsuccessful so far, as the fully activated toxins or free A1 subunits aggregate at low protein concentrations and have resisted crystallization (F. van den Akker, B. Hovey, and W. G. J. Hol, unpublished observations). Also, the structure of a proteolytically nicked but unreduced LT showed no major conformational difference from wild type (*12*). Such results suggest that conformational change must only occur upon full enzyme activation.

A1 loop regions have been suggested to serve as potentiators of activation-related conformational change (*13*). In the A/B toxin family, an active site loop composed of A-component residues (CT and LT 47−56, DT 39−47, PT 199−207, PE 458−463) occludes the active site in the proenzyme form, preventing substrate binding prior to activation (*3*, *8*, *13*). The crystal structure of an inactive R7K A-subunit LT holotoxin mutant showed that the active site loop in CT and LT had the potential to become disordered (*13*), leading the authors to propose a sequence of events, controlled by A1 loop regions, by which LT transitions from the proenzyme to the active enzyme. According to this proposal, nicking and reduction of the toxin cause the 25−36 loop, which contacts A1 and the A2 helix, to become flexible. An order-to-disorder transition in that loop breaks the contacts between Arg 25 and His (CT) or Tyr (LT) 55, suggested to be important for the stability of the 47−56 active site loop. This makes the active site loop flexible to permit the entrance of substrates into the active site. The CT/LT 25−36 loop, therefore, is proposed to be a key modulator of activity.

In the current paper, we investigate the hypothesis of van den Akker et al. in structural terms. Systematic mutagenesis of residues in the CT 25−36 loop led to the discovery of an A1:Y30S mutant that, while unnicked and unreduced, exhibits a similar level of activity to that of the wild-type, activated enzyme (Amaya et al., in preparation). In this study, we present crystal structures of the intrinsically active CTY30S mutant, providing the first structural views of an active form of CT or LT. To enable accurate structure−activity comparisons, we also independently determined the structure of wild-type CT at higher resolution and accuracy than were previously available (*10*). Our six new CT structures show an A2 tail conformation that differs markedly from that found in the original CT structure, with interesting implications for toxicity. In addition, the differences between CTY30S and wild-type CT structures permit further insight into the mechanism of CT/LT activation.

MATERIALS AND METHODS

Expression and Purification. Wild-type and Y30S variant cholera holotoxins were produced in *E. coli* BL21(DE3) cells carrying pARCT5 [wt, a derivative of the arabinose-inducible clone pARCT4 (*14*)] or pEIA154 (a derivative of pARCT4 with a site-directed mutation encoding Y30S). Bacteria were grown in Terrific broth to an OD_{600} of ∼1.0, and toxin gene expression was induced with 0.5% L-arabinose for 3 h before harvesting. Because the A and B subunits of CT naturally contain a periplasmic targeting signal, assembled holotoxin was isolated from a periplasmic extract, prepared by suspending the cell pellet in extraction buffer [$^1/_{40}$ culture volume containing 1 mg/mL polymyxin B sulfate in buffer G (50 mM Tris, pH 7.4, 200 mM NaCl, 1 mM EDTA, 3 mM NaN_3)] and incubating the suspension for 15 min at 37 °C. Toxin molecules were purified from the resultant extract on immobilized galactose resin (Pierce), eluted with 300 mM D-galactose (Fluka) in buffer G, followed by a Superdex 200 size-exclusion column (Pharmacia). Size-exclusion fractions containing holotoxin in either PBS, pH 7.0, or buffer G were then concentrated to 4.5−6 mg/mL for crystallization.

Crystallization and Cryoprotection. All crystals used in this study were obtained from sitting-drop vapor diffusion experiments conducted at room temperature.

CTY30S form 1 crystals were grown from drops containing 1.5 μL of protein solution in PBS, pH 7.0, and 1.0 μL of precipitant solution (14−20% PEG 2000 monomethyl ether, 100 mM MES, pH 6.0−7.0). CTY30S form 2 crystals grew from drops containing 1.5 μL of protein (in buffer G), 0.5 μL of 300 mM D-galactose (Fluka) in buffer G, and 1.0 μL of well solution (20% PEG 3350 + 100 mM sodium citrate). Plate-type CTY30S form 3 crystals were obtained from the same crystallization conditions as CTY30S form 1 but with the addition of 0.5 μL of kemptide solution [250 mM kemptide (Sigma), a heptapeptide artificial substrate for ADP-ribosylation [$K_M = 4.3$ mM (*15*)], in PBS pH 7.0] to the drop. CTY30S form 1 and form 3 crystals were transferred to 50% PEG 200 in artificial mother liquor before flash freezing, while form 2 crystals were cryoprotected with artificial mother liquor supplemented with 20% glycerol.

Two crystal forms of wild-type CT were used for data collection. Wild-type CT form 1 crystals grew from drops containing 1.5 μL of protein solution in buffer G, 0.5 μL of 300 mM D-galactose in buffer G, and 1.0 μL of precipitant [18−20% PEG 3350 + 150 mM $Mg(OAc)_2$]. A similar precipitant solution with a different salt (20% PEG 3350 + 200 mM lithium citrate) yielded elongated plate-type wild-type CT form 2 crystals under the same protein and galactose conditions. Prior to flash freezing for data collection, wild-type CT crystals were transferred to 20% ethylene glycol (form 1) or 20% glycerol (form 2) in the corresponding artificial mother liquor, supplemented with 50 mM D-galactose. While form 1 crystals were highly reproducible, wild-type CT form 2 crystals could not be reproduced. Despite extensive screening at room temperature and 4 °C, only galactose-supplemented drops yielded useful crystals. Crystals were also obtained from conditions suggested by Sigler et al., used for the initially published 2.4 Å wild-type CT structure (*10*, *16*), but these crystals only diffracted to a maximum resolution of 8 Å after optimization in our hands and were not used in this study.

Data Collection, Structure Determination, and Refinement. Data were collected at National Synchrotron Light Source (NSLS) beamline X12C (CTY30S form 1), Advanced Light Source (ALS) beamlines 5.0.2 (CTY30S form 3) and 8.2.2

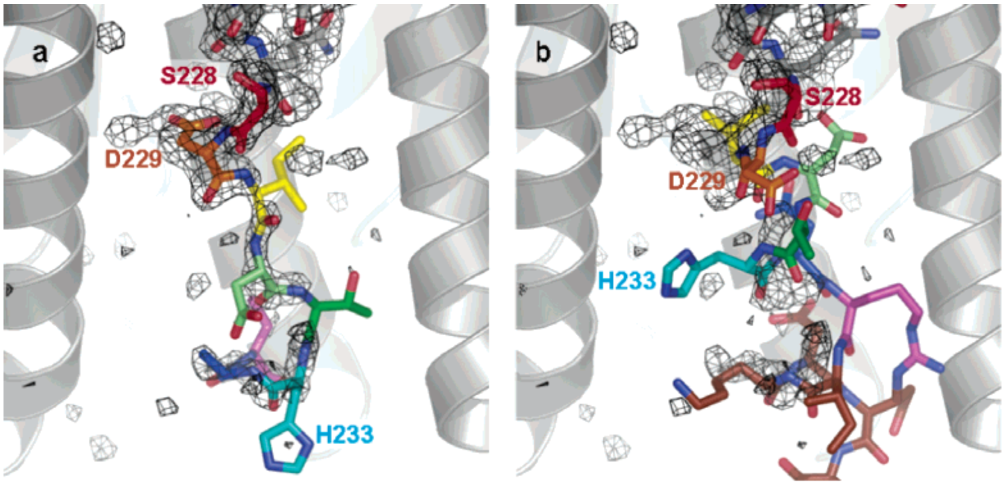

FIGURE 1: Comparison of the A2 tail between new and previously published (PDB ID 1XTC) wild-type CT structures. (a) The final model of wild-type CT form 1 molecule 2, with A2 residues in stick representation and the B_5 backbone in gray ribbons. Residues 228−235 are colored by residue number. (b) The A2 tail of 1XTC, viewed in the same orientation and with the same coloration as in (a). Residues 236−240 are shown in brown; these were included in the 1XTC model but were not seen in the new wild-type CT model. Shown in both (a) and (b) is the initial σ_A-weighted $F_o - F_c$ map (in black, 3σ contour) calculated for wild-type CT form 1 immediately after molecular replacement, at which point the model did not include A2 residues in this region. 1XTC begins to deviate significantly from the density starting at Asp 229 (orange), continuing a helical path, while the new structure follows the density to take a more extended path. Figures 1 and 3 were created using PyMOL (DeLano Scientific).

(wild-type CT forms 1 and 2), and Advanced Photon Source (APS) beamline 19ID (CTY30S form 2). All structures were processed and scaled with the HKL2000 suite (*17*) and solved by molecular replacement using the program MOLREP (*18*) from the CCP4 suite (*19*). CTY30S form 1 and form 3 structures were solved using the following procedure: (i) molecular replacement with a B_5 search model taken from a 1.25 Å CT B_5 structure (*20*) and then (ii) molecular replacement with the LT R7K A-subunit as a search model (*13*) while holding the top-scoring solution for B_5 fixed. The R7K mutant structure lacks the 47−56 active site loop and was additionally modified in our molecular replacement procedure by removing the A2 tail residues C-terminal to Lys 217, which sits above the B_5 pore. A possible reason the LT holotoxin could not be successfully used as a search model could be that its A subunit has a different relative orientation to B_5 than that found in the CT structures. The originally published CT structure was not used as a search model because of its significant deviations from ideal geometry statistics (Table 2). CTY30S form 2 and the wild-type CT structures were solved by molecular replacement with the refined CTY30S form 3 structure, again with the A2 tail truncated at Lys 217.

Solutions from MOLREP were subjected to restrained refinement in Refmac5 (*21*). Iterative rounds of model building in Xtalview (*22*) and refinement in Refmac5 were used to substitute LT residues with CT residues when applicable, add missing residues and waters, and remove atoms or residues not supported by density. Strong positive density in the B_5 pore enabled the unambiguous placement of A2 tail residues not included in the search model (Figure 1). Placement of galactose molecules, when supported by density, was guided by superposition of the target structure with that of LT complexed with galactose [PDB ID 1LTA (*23*)]. As the models neared completion, TLS refinement carried out in Refmac5 further lowered *R*-values. Final refinement statistics are presented in Table 1.

RESULTS

Quality of the CTY30S Structures. CTY30S structures were obtained from three crystal forms, each containing one AB_5 heterohexamer per asymmetric unit. These crystals diffracted to 2.5, 1.75, and 2.1 Å, respectively, and were refined to an R_{cryst}/R_{free} of 0.195/0.262, 0.161/0.191, and 0.177/0.224, respectively (Table 1). The 1.75 Å structure of CTY30S form 2, a cocrystal with galactose, is the highest resolution structure yet published for the CT or LT heterohexamer. Despite the fact that CTY30S form 3 was crystallized in the presence of the heptapeptide substrate kemptide, density that could be interpreted as a kemptide molecule was not found in the active site or in crystal-packing contacts of the CTY30S form 3 structure. Final models from all three structures exhibit excellent stereochemistry and geometry, as determined by RMSD values from ideality (Table 1) and evaluation of the models by PROCHECK (*24*) (Table 2). Structures from the three CTY30S crystal forms mutually agree, with the RMSD over all C^α atoms being 1.0 Å between forms 1 and 2 and 0.5 Å between forms 2 and 3.

Although the toxin molecules observed in the three CTY30S crystal forms have not undergone the activational modifications required by wild-type CT for full activity, the structures represent active toxin since unnicked and unreduced CTY30S exhibits enzymatic activity comparable to fully nicked and reduced wild-type CT (Amaya et al., in preparation). Crystals of CTY30S were shown to contain unnicked toxin by a reducing SDS−PAGE analysis of dissolved crystal samples (data not shown). Though residues near the A1−A2 cleavage site were not visible in any CTY30S electron density maps and were left out of the models, similar disorder around the cleavage site has been observed in all other structures of unnicked LT (*11*, *13*, *23*, *25*, *26*). In all three CTY30S structures, the A1:187−A2:199 disulfide bond is clearly intact and shows continuous density at a 3σ contour level in σ_A-weighted $2F_o - F_c$ maps.

Table 1: Data Collection and Refinement Statistics[a]

	wild-type CT		CTY30S		
	form 1	form 2	form 1	form 2	form 3
data collection					
λ (Å)	1.0781	1.0781	1.0414	1.0000	0.9800
space group	$P2_1$	$P2_12_12_1$	$P2_1$	$P2_12_12_1$	$P2_1$
unit cell dimensions a, b, c (Å)	59.9, 108.2, 123.0	60.2, 111.0, 123.6	58.8, 85.2, 71.3	60.1, 111.9, 124.7	60.1, 107.4, 66.0
unique β angle (deg)	95.9		104.5		91.3
max resolution (Å)	1.9	2.6	2.5	1.75	2.1
mosaicity (deg)	0.607	0.479	1.108	0.393	1.541
unique reflections	122355	24872	23518	81774	46322
completeness (%)	99.1 (97.1)	94.7 (96.7)	99.2 (98.7)	95.5 (73.2)	99.6 (99.8)
average I/σ[b]	14.5 (2.85)	10.2 (2.75)	12.2 (2.5)	25.3 (3.37)	12.1 (3.3)
redundancy	3.6	3.8	3.7	6.1	3.2
R_{sym} (%)[c]	8.3 (39.1)	13.3 (54.6)	10.6 (48.4)	6.8 (29.1)	9.6 (39.2)
refinement					
protein residues	1488	738	731	733	723
water molecules	748	59	94	603	404
sodium ions	2	1	1	1	1
galactose molecules	2	5		5	
R_{cryst}/R_{free}[d]	0.167/0.205	0.213/0.260	0.195/0.262	0.161/0.191	0.177/0.224
RMSD from ideality					
bond lengths (Å)	0.013	0.009	0.009	0.010	0.012
bond angles (deg)	1.404	1.226	1.215	1.227	1.282
chirality	0.104	0.067	0.070	0.077	0.076

[a] Data collection and refinement statistics for the structures presented herein. Numbers in parentheses indicate values for the highest resolution shell. [b] I/σ is the mean reflection intensity divided by the average estimated error. [c] $R_{sym} = (\sum|I_{hkl} - \langle I\rangle|)/\sum I_{hkl}$, where the average intensity $\langle I\rangle$ is taken over all symmetry equivalent measurements and I_{hkl} is the measured intensity for any given reflection. [d] $R_{cryst} = ||F_o| - |F_c||/|F_o|$, where F_o and F_c are the observed and calculated structure factor amplitudes, respectively. R_{free} is equivalent to R_{cryst} but is calculated for 5% of the reflections chosen at random and omitted from the refinement process.

Table 2: Peptide Backbone Geometry Analysis[a]

	wtCT		CTY30S			
residues in Ramachandran plot regions (%)	form 1	form 2	form 1	form 2	form 3	1XTC
most favored	93.1	91.9	90.2	93.6	92.1	75.3
additionally allowed	6.9	7.9	9.8	6.4	7.9	19.8
generously allowed	0	0.2	0	0	0	3.5
disallowed	0	0	0	0	0	1.3

[a] Peptide backbone geometry analysis, shown as percent of total residues in the final model, was evaluated by a Ramachandran plot (using PROCHECK) for the wild-type CT and CTY30S structures and the previously published wild-type CT structure (PDB ID 1XTC) (*10*).

The four C-terminal A2 residues containing the KDEL sequence were not clearly defined by electron density maps in any of the CTY30S structures and are not included in the final models. This region has been implicated in retrograde transport of CT and LT from the Golgi to the ER, one leg of the complex journey taken by these toxins to travel from the intestinal lumen to the cytosolic face of the epithelial cell plasma membrane (*27*, *28*). While this region has consistently been disordered in structures of LT (*11*−*13*, *23*, *25*, *26*), KDEL residues were included in the previously published wild-type CT structure with the mention that their densities were incomplete (*10*).

Loop Residues. Residues in the 25−36 "activation loop" were ordered in the originally determined wild-type CT structure and in wild-type LT structures but displayed mostly higher than average *B*-factors in wild-type LT structures. These residues were included in the molecular replacement model used for CTY30S structure determinations, but density in the CTY30S structures did not support the inclusion of activation loop residues in the final models, suggesting that the activation loop is disordered in CTY30S (Figure 2). Activation loop disorder varies slightly among the crystal forms; in CTY30S forms 1 and 3, residues 26−36 are disordered, whereas in CTY30S form 2, residues 29−36 are disordered but Gly 26, Gln 27, and Ser 28 are observed and exhibit relatively high thermal parameters.

In contrast to the activation loop, the 47−56 active site loop is mostly ordered in the structures of CTY30S forms 1 and 2 and occludes the active site as in wild-type CT and LT (Figure 2). This loop was not included in the molecular replacement model but asserts its presence with strong positive density in the CTY30S structures. The active site loop appears to be slightly flexible in CTY30S form 3, crystallized in the presence of kemptide, with poor or uninterpretable density for residues 47−52 but strong density for residues 53−56. In all three cases, the His 55−Arg 25 backbone hydrogen bond between the activation and active site loops is intact, and Arg 54 forms a salt bridge with Glu 112 in each CTY30S structure, limiting accessibility of substrate to this essential catalytic residue.

The A2 Tail. In all CTY30S structures, A2 adopts an extended conformation as it passes through the B_5 pore, quite distinct from the helical-type tail reported in the previously published 2.4 Å wild-type CT structure (*10*). This portion of the A-subunit is unlikely to affect the A1 activation and active site loop conformations, being remote from these regions and sequestered inside the B_5 pore. However, to obtain an entirely correct view of the tail conformation and to provide a more geometrically sound model for comparison with CTY30S, we independently determined the structure of wild-type CT.

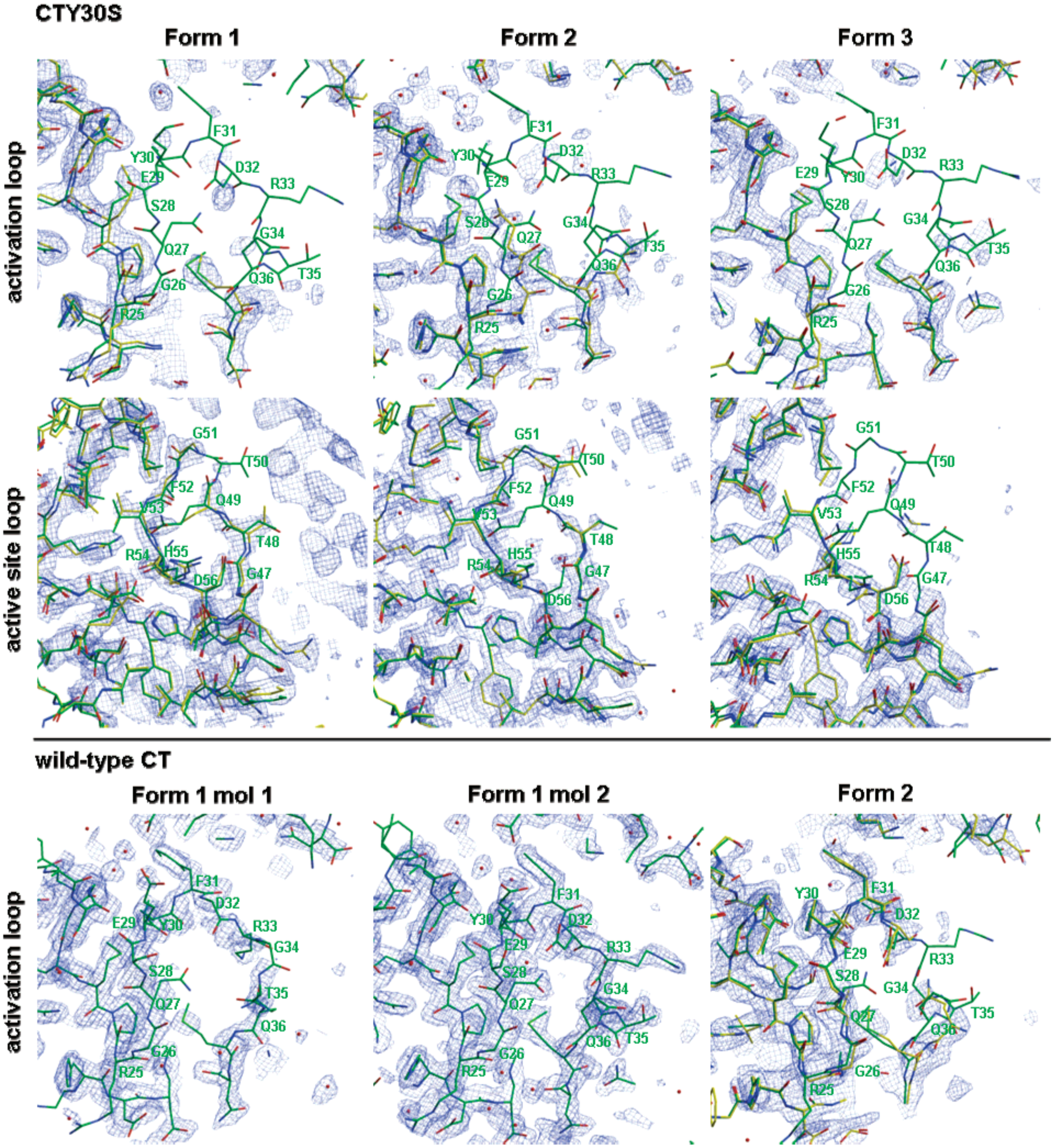

FIGURE 2: Comparison of A1 loops between CTY30S and wild-type CT structures. CTY30S models (in yellow, upper and middle panels) are superposed with the wild-type CT form 1 molecule 2 (green) to illustrate where loops are expected to be. The respective σ_A-weighted $2F_o - F_c$ omit map (1σ contour) is shown in each panel. The 25−36 activation loop is disordered in the CTY30S structures, while the 47−56 active site loop displays varying levels of order. Both loops are ordered in wild-type CT, with the minor exception of residues 33−35 of the wild-type CT form 2 activation loop (bottom right, wild-type CT form 2 model in yellow). Created with Raster3D (*36*).

Quality of the New Wild-Type CT Structures. Wild-type CT structures were obtained from two crystal forms, both cocrystals with galactose, a B-subunit ligand. The 1.9 Å structure obtained from form 1 wild-type CT crystals contains two AB_5 toxin molecules per asymmetric unit, yielding an R_{cryst} of 16.7% and an R_{free} of 20.5% (Table 1). The final 2.6 Å structure of wild-type CT form 2 contains one AB_5 toxin molecule per asymmetric unit with an R_{cryst} of 21.3% and an R_{free} of 26.0% (Table 1). Interestingly, wild-type CT form 2 has unit cell dimensions nearly identical to those of CTY30S form 2 (Table 1). The final models for each crystal form display excellent stereochemistry and geometry as determined by RMSD values from ideality and Ramachandran plots calculated by PROCHECK (*24*) (Tables 1 and 2). The three wild-type CT models agree very well with each other. Superpositions of all C^α atoms of wild-type CT form 1 molecule 2 and wild-type CT form 2 onto wild-type CT form 1 molecule 1 yield RMSD values of 0.6 and 0.4 Å, respectively. As in CTY30S structures, residues near the A1−A2 cleavage site and at the C-terminus of the A2 tail were omitted from the structures due to poor or incomplete density.

Galactose Binding. In this study, wild-type CT crystals suitable for data collection were only obtained by cocrystallization with galactose. The crystals exhibited different unit cell dimensions than the previously determined wild-

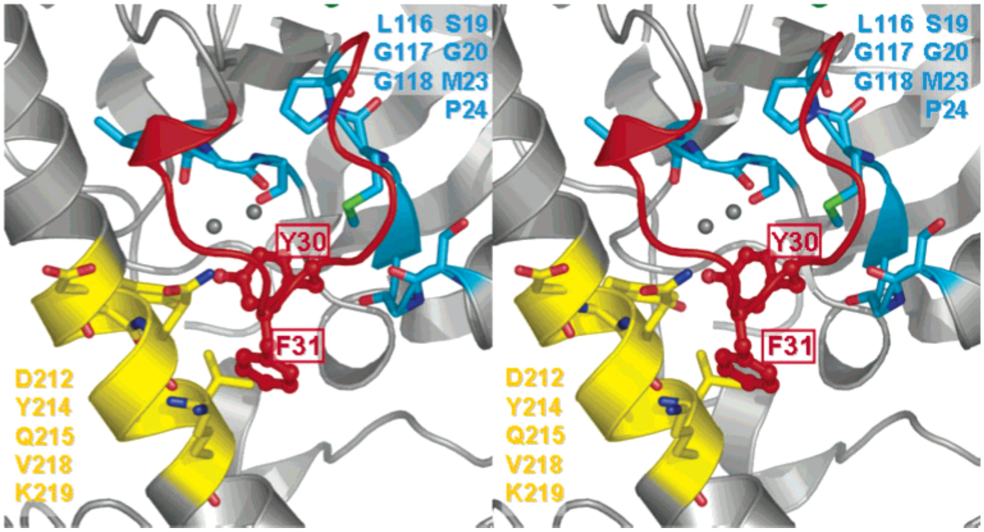

FIGURE 3: Stereoview of regions contacted by the activation loop in wild-type CT. Backbones of important regions are shown as colored ribbons (activation loop, red; A1 contact region, blue; A2 contact region, yellow), with side chains of residues that contact the loop displayed as correspondingly colored stick models. Only Tyr 30 and Phe 31 are displayed, in ball-and-stick representation, from the activation loop for clarity. Table 3 lists contacts specifically made by Tyr 30. Wild-type CT form 1 molecule 2 was used in this representation; this area is highly superimposable between both molecules in the form 1 crystal structure.

type CT structure (*10*) and, in the case of form 1 wild-type CT, diffracted to higher resolution (Table 1). It is unlikely that the A-subunit of galactose-bound CT will exhibit significant conformational change relative to unliganded CT, since residues involved in galactose binding are located on the opposite face of B_5 from A1 (*23*), and neither these residues nor galactose molecules are involved in crystal contacts with A1 in the wild-type CT crystal forms discussed herein. Also, a previous study which similarly obtained LT–galactose cocrystals in a different crystal form than "apo" LT observed no major conformational difference in the A-subunit between apo and galactose-complexed LT (*23*). Thus, the A-subunits of these wild-type CT crystal structures are suitable for comparison with A-subunits of CT and LT structures not complexed with galactose, such as CTY30S forms 1 and 3.

Loops in Wild-Type CT. The availability of multiple structures of each CT species in different crystal forms enables an analysis of the loop conformations in different crystal lattices. The fact that the activation loop is consistently disordered in CTY30S structures but is ordered in wild-type CT structures, despite different packing environments among the crystal forms, indicates that the activation loop is not likely to be affected by crystal packing interactions in these structures.

In all wild-type CT structures, both the 25–36 activation loop and 47–56 active site loop are ordered, with a minor exception of the activation loop of wild-type CT form 2. In this structure, the density for A1 residues 33–35 was weak and discontinuous, and these residues were not included in the final model (Figure 2). The conformation adopted by the visible activation loop residues 26–28 in the CTY30S form 2 structure differs markedly from that observed in the new wild-type structures, by as much as 5 Å at the C^{α} of Ser 28 (Figure 2).

The activation loop buries a 725 $Å^2$ hydrophobic patch in wild-type CT molecules, distributed between the face of A1 and the A2 helix (Figure 3). The A1 contact patch consists of A1 residues N-terminal to the 25–36 activation loop, Ser 19, Gly 20, Met 23, and Pro 24, and A1 residues Leu 116, Gly 117, and Gly 118. The A2 contact patch is made up of residues from a portion of the extended A2 α-helix facing A1: Asp 212, Tyr 214, Gln 215, Val 218, and Lys 219. Tyr 30 is the only residue in the activation loop that contacts residues in both regions and additionally makes a water-mediated hydrogen bond to Asn 93 $N^{\delta 2}$ with its phenolic oxygen (Table 3). The hydrophobic patch is highly superimposable between wild-type CT and CTY30S, with the highest RMSD among the structures being 0.4 Å over 12 C^{α} atoms between wild-type CT form 1 molecule 2 and CTY30S form 1.

Table 3: Contacts Made by Tyr 30 Atoms to Residues outside the Activation Loop[a]

Tyr 30 atom	contacts
N	Met 23 S^{δ}, Ser 19 O*
C^{α}	Met 23 S^{δ}
C^{β}	Gly 20 O, Met 23 C^{ϵ}
$C^{\delta 1}$	Met 23 C^{ϵ}, Gly 117 O
$C^{\epsilon 1}$	Gly 117 O
$C^{\epsilon 2}$	Gln 215 C^{γ}
OH	Asn 93 $N^{\delta 2}$**, Leu 116 O**, Gly 118 O**, Tyr 214 $C^{\delta 2}$, Tyr 214 $C^{\epsilon 2}$
C	Gln 215 $N^{\epsilon 1}$

[a] Contacts are van der Waals interactions (3.9 Å cutoff) unless noted to indicate a hydrogen bond (*) or a water-mediated hydrogen bond (**). Contacts listed are common to both molecules of the high-resolution wild-type CT form 1 structure.

Aside from the contacts made within the Y30/F31 hydrophobic patch, the only other contacts made by activation loop residues are those between Arg 25 and active site loop residues. In CT, these include (i) van der Waals contacts between Arg 25 C^{α} and C^{β} and His 55 $N^{\epsilon 2}$ and between Arg 25 N^{ϵ} and C^{ζ} and His 55 $C^{\epsilon 1}$, (ii) a hydrogen bond between the Arg 25 backbone nitrogen and the His 55 carbonyl oxygen, and (iii) a salt bridge between Arg 25 and Asp 56 side chains. These are the only direct structural contacts between the activation and active site loops in wild-type CT. LT makes more extensive side-chain contacts between Arg 25 and Tyr 55. Interestingly, contacts between Arg 25 and

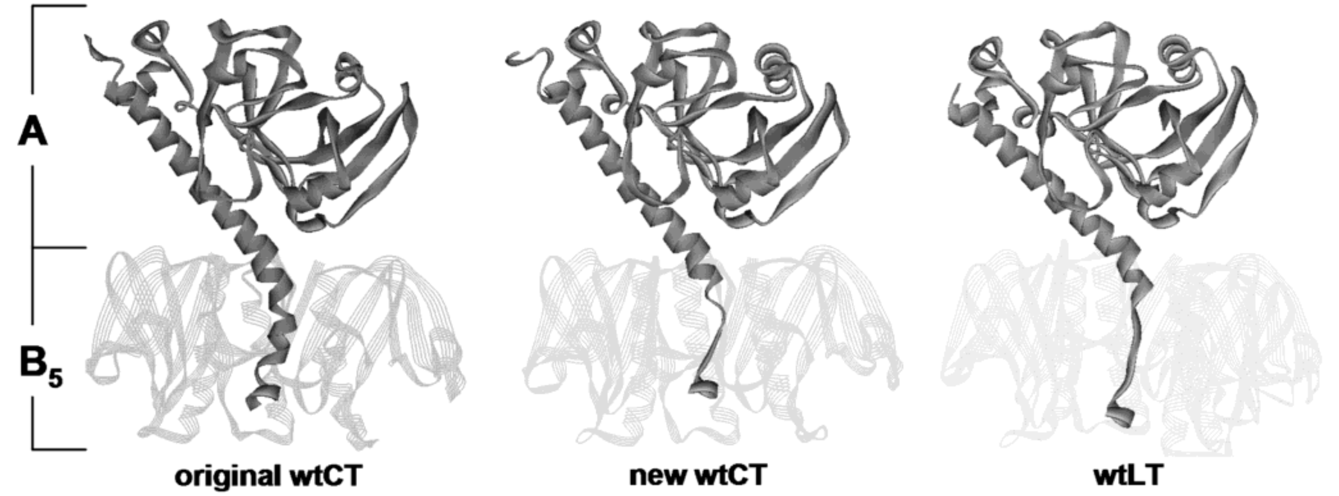

FIGURE 4: Comparison of CT and LT holotoxin structures in similar orientations. The original CT structure (*10*) is shown on the left, wild-type CT form 1 molecule 1 is in the middle, and the 1.9 Å structure of wild-type LT (*11*) is on the right. B_5 is shown in semitransparent ribbons with front subunits removed to reveal the A2 tail detail. While the new wild-type CT structure (middle) shows a different A2 tail conformation from the previously published wild-type CT structure (left), the new CT tail conformation (middle) still differs from the elongated tail of wild-type LT (right). Created with ViewerLite (Accelrys).

the active site loop are mostly preserved in CTY30S structures, suggesting that direct contacts may not be important in transmitting the status of the activation loop to the active site loop.

Comparison of Old and New Wild-Type CT Structures. The three new wild-type CT structures display considerably improved geometry over the previously published CT structure (Table 2) and a strikingly different conformation of the A2 tail as it threads through the B_5 pore. The A2 tail from the previously published CT structure did not fit well into our initial difference density maps from the molecular replacement solution in this region, being slightly translated with respect to density between Ser 224 and Ser 228 but adopting an entirely different conformation than described by the density starting at Asp 229 (Figure 1). In our structures, the CT A2 tail adopts an elongated conformation through the B_5 pore, deviating from the helical conformation reported for the previously published wild-type CT structure at Tyr 226, where the extended A2 α-helix stops (Figure 1). The new A2 backbone makes a curve through Ser 228 and Asp 229 before taking an almost straight path to Thr 232, where it ends in a short, one-turn helix very similar to that of LT (Figure 4). This tail conformation is agreed upon by the six independent CT structures presented in this paper, among which the highest pairwise C^{α} RMSD over residues 226−235 is 0.33 Å, compared to a C^{α} RMSD of 3.3 Å between the previously determined wild-type CT structure and the new wild-type CT molecules over the same residues.

Comparison between Wild-Type CT and Wild-Type LT Structures. Though the new wild-type CT tail is elongated, it is not identical to the elongated A2 tail conformation of wild-type LT. Once the wild-type LT A2 α-helix ends at Tyr 226, the LT tail then immediately begins a nearly vertical descent through the pore, ending in a one-turn α-helix (Figure 4). Without a bend around residues 228 and 229, the LT tail extends further through the pore toward the receptor-binding site of B_5 than that of CT. The distance between Val 218 C^{α}, just above the pore, and Ile 236 C^{α} is 33.0 Å in LT, while the corresponding distance is 30.5 Å in CT.

DISCUSSION

The three crystal structures of CTY30S reported herein present the first opportunity to structurally characterize an active form of CT. Amaya et al. demonstrated that proteolytic nicking and disulfide bond reduction are not required for CTY30S to exhibit catalytic activity comparable to that of fully activated wild-type CT (Amaya et al., in preparation). Thus, it is likely that conformational differences between wild-type CT and CTY30S reflect conformational changes that occur upon activation of wild-type CT. Because CTA and LTA share over 80% sequence identity and catalyze an identical reaction on the same substrate, it is probable that insight into the activation mechanism of CT, provided by CTY30S structures, also holds for LT.

The only major structural changes observed between wild-type CT and CTY30S occur in the level of flexibility found in the activation and active site loops. That this seemingly minor change appears to be the difference between proenzyme and active enzyme forms is not surprising, as similar behavior has been observed in related ADP-ribosylating toxins. In structures of DT and PE, the authors note that the overall structure of the catalytic domain is preserved between the activated toxin and its proenzyme, with the only exceptions being in loop regions (*3*, *8*).

The Activation Loop in CT and LT. A previous study suggested that the 25−36 activation loop may play a crucial role during the transition from inactive proenyzme to activated CT and LT (*13*). The wild-type CT structures presented here, together with the published structures of wild-type and mutant forms of LT, provide an abundance of structural information to characterize the properties of this loop.

B-Factors along the activation loop are higher than the average *B*-factors for the A1 subunits of the CT/LT structures, suggesting that this loop already has a tendency toward disorder (Figure 5). Missing density in the wild-type CT form 2 structure for residues 33−35 further underscores the high level of thermal motion naturally present in this loop (Figure 2). A graph of CT and LT main-chain *B*-factors

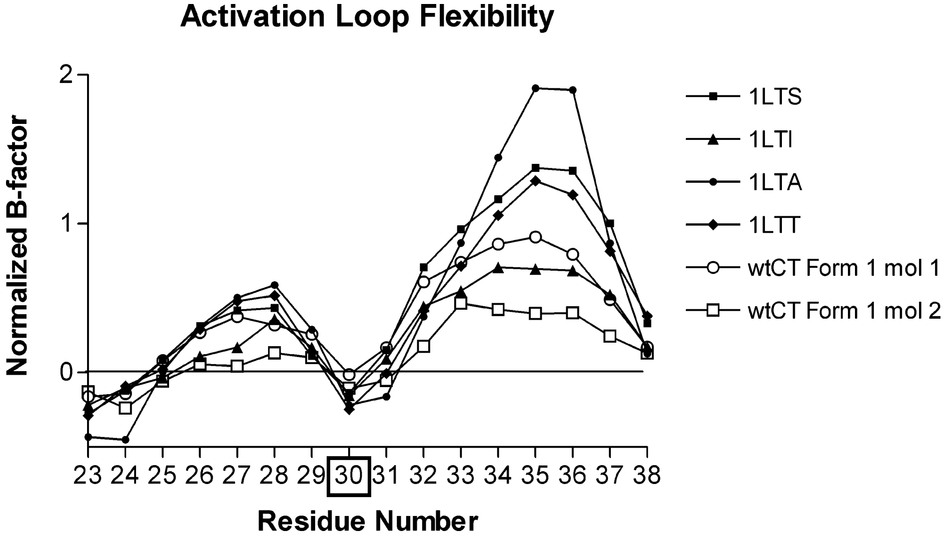

FIGURE 5: Normalized C$^{\alpha}$ *B*-factor plot for the 25−36 activation loop from published wild-type LT structures [PDB IDs 1LTS (*11*), 1LTI (*26*), 1LTA (*23*), and 1LTT (*37*)] and the CT structures presented herein. The loop can be divided into two flexible regions (peaks) separated by a small local *B*-factor minimum at Tyr 30. Created with GraphPad Prism (GraphPad Software).

along the 25−36 activation loop, however, shows that *B*-factors are not uniformly high, and instead the loop consists of two regions of high local *B*-factors separated by a small region, centered at Tyr 30 C$^{\alpha}$, of low local *B*-factors (Figure 5).

The propensity to disorder in the activation loop is further underscored by an inspection of the amino acid composition of the loop (CT 25−36, RGQSE**YF**DRGTQ; LT 25−36, RGHNE**YF**DRGTQ), which is highly biased toward hydrophilic residues. The only hydrophobic residues in the loop, Tyr 30 and Phe 31, bury 450 and 394 Å^2, respectively, together representing over half of the buried surface area of the entire activation loop. In particular, C$^{\delta}$, C$^{\epsilon}$, and C$^{\zeta}$ side-chain atoms of Tyr 30 pack tightly against both the A1 and A2 regions of the pocket buried by the loop (Figure 3, Table 3). Tyr 30 and Phe 31 are conserved between LT and CT, as are all of the residues with which they interact.

These structural observations suggest that Tyr 30 acts as a “molecular snap” which mediates the flexibility of the activation loop. When the Tyr 30 aromatic group is replaced with a Ser, this smaller residue is unlikely to be able to make the important contacts made by the outer atoms of the Tyr 30 side chain. As a result, the mostly hydrophobic pocket that anchors Tyr 30 and Phe 31 will not be optimally filled by the small hydrophilic group of the newly introduced Ser. The activation loop of CTY30S, now containing only one hydrophobic residue in the dodecapeptide, can favorably interact with the solvent and thus become completely disordered. Tyr 30 may be more important for loop stabilization than Phe 31 because a F31S mutant, though capable of some activity without proteolytic nicking or reduction, was not as active as the Y30S mutant (Amaya et al., in preparation). This is consistent with the larger buried surface area of Tyr 30 relative to Phe 31.

Why Is CTY30S Active? Though assays clearly show that CTY30S is intrinsically active (Amaya et al., in preparation), the active site loop is ordered in CTY30S form 1 and 2 crystal structures, occluding the active site as in wild-type CT. How can the intrinsic activity of CTY30S be explained with these seemingly contradictory observations? Inspection of structures of related ADP-ribosylating toxins DT and PE shows that, like wild-type CT, the active site loop is ordered in unactivated DT, PE, and PT (*3*, *4*, *7*). The active site loop is also ordered in apo, activated DT, as well as in a cocrystal structure of DT with ApUp, a nonsubstrate dinucleotide that differs from NAD$^+$ in its nucleoside linkage and its use of uracil in place of nicotinamide (*8*, *29*). However, when NAD$^+$ or β-methylenethiazole-4-carboxamide adenine dinucleotide, a nonhydrolyzable NAD$^+$ analogue, is bound to fully activated DT or PE, respectively (*2*, *9*), the active site loop becomes disordered. Thus, the structures of other ADP-ribosylating toxins point to a possible mechanism where activation does not completely disorder the active site loop but, instead, increases mobility (as seen in CTY30S form 3) and thereby *predisposes* the active site loop to disorder when substrates, or molecules that are very nearly identical to the toxins’ natural substrates, are present.

The structural evidence available from CTY30S and related toxins thus suggests that the active site loop order-to-disorder transition occurs only when two conditions are met: (1) toxin activation has occurred, and (2) substrate is present. Individually, each of these conditions is necessary but not sufficient for active site loop disorder. When both conditions are met, as observed in the substrate-bound structures of DT and PE, the active site loop becomes disordered, the active site is accessible, and substrate binding occurs. Partial disorder in the active site loop of CTY30S form 3 suggests that the CT active site loop also has this propensity to become disordered in the presence of substrate.

Role of the Activation Loop in the Activation Mechanism. Activation loop disorder is the only major conformational difference between the high-resolution wild-type CT structures and all the CTY30S structures. This feature is thus likely to be a key factor for the difference in intrinsic activity between wild-type CT and constitutively active CTY30S, suggesting that disorder in this loop is necessary for the transition between proenzyme and active enzyme. This raises the question as to how, upon nicking and reduction, the activation loop becomes disordered in activated wild-type toxin, since (i) Tyr 30 is present and firmly buried against the pocket formed by A1 and A2 residues in unactivated CT and LT, albeit with high *B*-factors in the surrounding loop residues, and (ii) the positions of the A1 and A2 helix regions interacting with Tyr 30 are very similar in wild-type CT and CTY30S. It seems unlikely that proteolytic nicking and disulfide bond reduction directly affect the activation loop, as the site of these modifications lies over 20 Å away from closest activation loop residues.

One possible way that nicking and reduction of the A-subunit could lead to activation loop disorder would be an increase in mobility or a slight loosening of the A2 α-helix, which makes up one wall of the Y30/F31 pocket (Figure 3). The A2 helix appears to have some propensity to break its interface with A1: though the A1:A2 interface buries ∼2200 Å^2 in the wild-type structure, ∼40% of this interaction interface is composed of water-mediated contacts. However, the remaining ∼1200 Å^2 of the interface is held together by protein−protein interactions, lending structural evidence to the experimental observation that the A-subunit in cleaved and reduced form resists large structural changes in physiological buffers, with dissociation into A1 and A2 components only occurring in the presence of 4−6 M urea (*5*). A1:Y30S also remains noncovalently associated with A2 and B$_5$ after nicking and reduction in a mild aqueous environment in a manner which is indistinguishable from that for wtCT (data not shown), showing that intrinsic disorder in the activation loop is not sufficient to break the A1−A2 packing interactions. In vitro, therefore, activation may not be enough to completely remove the A2 helix from A1. It is possible, however, that nicking and reduction make the interaction of A2 with A1 less firm, even though we observe that the average coordinate position of A2 has not changed between wild-type and Y30S CT structures. Increased mobility around essentially the same average position of the A2 helix could allow the free energy difference between a fixed and a flexible conformation of the activation loop to favor that of the flexible conformation.

In light of the route proposed for in vivo transport of CTA1 into the cytosol, it makes sense that, in vitro, the A-subunit must be subjected to conditions in which unfolding could occur to separate A1 from A2. To reach the cytosol from the ER, CT and other ADP-ribosylating toxins have been speculated to make use of the Sec61p retrotranslocation machinery, which transports misfolded proteins from the ER to the cytosol for degradation (*30*). Several studies have shown that CTA1 can masquerade as a misfolded protein and gain access to the cytosol using this machinery (*31*−*33*). This suggests that, for transport to the cytosol, A1 must completely separate from A2. The ER, as a locus for the folding of certain proteins, may assist the escape of A1 from A2 by providing a chaperone for unfolding of A1, which then could pass unfolded A1 to the Sec61p machinery. Tsai et al. have already suggested that protein disulfide isomerase can act as an unfoldase (*34*), though it is possible that another protein could assist in this task. If ER-assisted CT activation encourages physical separation and departure of A1 from A2, an entire wall of the Y30/F31 pocket would be removed, exposing 36% of surface area buried by Y30 and F31 to solvent and potentially destabilizing the Y30/F31 pocket to allow activation loop disorder.

Proposed Activation Mechanism. The first crystal structures of an active Y30S mutant cholera toxin, when compared with the new structures of unactivated wild-type cholera toxin, allow us to sketch possible structural transitions that take place during the CT/LT activation process (Figure 6).

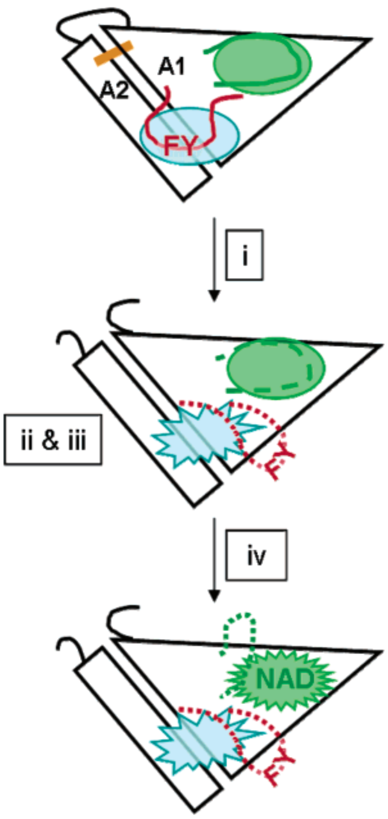

FIGURE 6: Schematic illustration of the proposed in vitro activation mechanism and its effects on A1 and A2. Top: A1 (triangle) and A2 (rectangle) prior to activation, with covalent connections via their mutual peptide chain (black loop) and disulfide bond (orange line) intact. Middle: Activation severs the peptide chain and disulfide bond, which causes an indirect structural change in the environment of Y30 and F31 or in the hydrophobic patch (blue) contacted by these residues. This change results in activation loop (red) disorder, which in turn predisposes the active site loop (green) toward disorder upon binding NAD (bottom). In vivo, it is likely that A1 and A2 are physically separated shortly after reduction of the A1−A2 disulfide bond in the ER, simplifying the concept of Y30/F31 pocket disruption.

(i) Proteolytic nicking and reduction of the A-subunit Cys 187−Cys 199 disulfide bond sever the covalent connections between A1 and A2. These modifications encourage some increase in mobility of the A2 helix with respect to A1.

(ii) The resulting increased mobility of one wall of the Y30/F31 pocket causes the activation loop to become disordered. In vitro, this may occur due to a weakening of the A1−A2 interface because of nicking and reduction, allowing Y30 and F31 to move away from the pocket, driven by the free energy gain of the remaining hydrophilic residues of the loop when they become fully solvent-exposed. In vivo, this natural weakening may be further assisted by molecular chaperones in the ER that unfold the A-subunit to cause separation of A1 from A2, thereby decreasing significantly the number of contacts that had held the activation loop, and Y30 in particular, in place.

(iii) Disorder in the activation loop causes a generalized increase in flexibility of the A-subunit, affecting the active site loop through indirect structural contacts. Activation loop disorder renders the toxin active by predisposing the active site loop to become flexible and expose active site residues upon substrate binding.

(iv) Substrate binding displaces the active site loop because of the enhanced mobility of the loop, causing the active site loop to become fully disordered.

This activation mechanism is similar to that proposed previously for LT by van den Akker et al. (*13*), but unlike that mechanism, structures of CTY30S and related ADP-ribosylating toxins provide additional information to suggest that disorder in the activation loop is both necessary and sufficient for toxin activity and that the active site loop only becomes disordered in the presence of substrate (*8*, *9*).

A2 Tail Conformation. All six crystal structures of CT presented in this study exhibit an elongated conformation of A2 through residues 226−236, in contrast to the helical-type tail proposed by the originally published structure of wild-type CT (*10*) (Figure 4). This difference has two intriguing physiological implications.

First, an unresolved issue from the previous CT helical-tail model was that the KDEL ER-retention signal sequence remained tucked into the B_5 pore, mostly inaccessible to solvent and, presumably, to the KDEL receptor. Though the KDEL sequence is disordered in the new CT structures, the new elongated tail conformation observed in these structures positions this sequence to extend into solvent at the exit of the B_5 pore, facilitating its proposed interaction with the KDEL receptor (Figure 4).

Second, it has been proposed that the entire difference in in vitro activity between CT, which causes cholera, and LT, which causes the less severe traveler's and children's diarrhea, can be attributed to an 11-residue section of A2 amino acids "buried" in the pore of B_5, from Tyr 226 to Ile 236 (*35*). A study of A2 tail chimeras of CT and LT concluded that the conformation of the CT tail was responsible for enhanced holotoxin stability, presumably because of a larger number of interactions made by the CT tail as compared to the LT tail. With the structures available at the time, explaining this difference from a conformational basis was relatively straightforward, as overall A2 tail conformations were so obviously different between CT and LT. Though the new CT tail model is elongated like that of LT, the conformations of the CT and LT tails are clearly different (Figure 4). Because the A2 helix of CT extends two residues past that of LT and because the CT tail exhibits a gentle curvature around Asp 229, the new CT tail also makes more interactions with B_5 than the LT tail does. Thus, our new model is still compatible with conclusions made by Rhodighiero et al. (*35*).

ACKNOWLEDGMENT

We thank the staffs of beamline 8.2.2 at the ALS and beamline 19ID at the APS for access to superb synchrotron facilities. ALS, APS, and NSLS are supported by the U.S. Department of Energy. We are grateful to Drs. Ethan Merritt, Christophe Verlinde, and Erkang Fan for helpful discussions, to Dr. Francis Athappilly for expert computer support, and to Stewart Turley and Dr. Jim Pflugrath for assistance with data collection. We are indebted to Dr. Douglas R. Davies for technical advice and critique of the manuscript.

REFERENCES

1. Widdus, R. (2001) Public-private partnerships for health: their main targets, their diversity, and their future directions, *Bull. W.H.O. 79*, 713−720.
2. Bell, C. E., and Eisenberg, D. (1996) Crystal structure of diphtheria toxin bound to nicotinamide adenine dinucleotide, *Biochemistry 35*, 1137−1149.
3. Wedekind, J. E., Trame, C. B., Dorywalska, M., Koehl, P., Raschke, T. M., McKee, M., FitzGerald, D., Collier, R. J., and McKay, D. B. (2001) Refined crystallographic structure of *Pseudomonas aeruginosa* exotoxin A and its implications for the molecular mechanism of toxicity, *J. Mol. Biol. 314*, 823−837.
4. Stein, P. E., Boodhoo, A., Armstrong, G. D., Cockle, S. A., Klein, M. H., and Read, R. J. (1994) The crystal structure of pertussis toxin, *Structure 2*, 45−57.
5. Mekalanos, J. J., Collier, R. J., and Romig, W. R. (1979) Enzymic activity of cholera toxin. II. Relationships to proteolytic processing, disulfide bond reduction, and subunit composition, *J. Biol. Chem. 254*, 5855−5861.
6. Masignani, V., Pizza, M., and Rappuoli, R. (1999) in *Bacterial Protein Toxins* (Aktories, K., and Just, I., Eds.) pp 21−44, Springer, Berlin.
7. Bennett, M. J., Choe, S., and Eisenberg, D. (1994) Refined structure of dimeric diphtheria toxin at 2.0 Å resolution, *Protein Sci. 3*, 1444−1463.
8. Bell, C. E., and Eisenberg, D. (1997) Crystal structure of nucleotide-free diphtheria toxin, *Biochemistry 36*, 481−488.
9. Li, M., Dyda, F., Benhar, I., Pastan, I., and Davies, D. R. (1996) Crystal structure of the catalytic domain of *Pseudomonas* exotoxin A complexed with a nicotinamide adenine dinucleotide analog: implications for the activation process and for ADP ribosylation, *Proc. Natl. Acad. Sci. U.S.A. 93*, 6902−6906.
10. Zhang, R. G., Scott, D. L., Westbrook, M. L., Nance, S., Spangler, B. D., Shipley, G. G., and Westbrook, E. M. (1995) The three-dimensional crystal structure of cholera toxin, *J. Mol. Biol. 251*, 563−573.
11. Sixma, T. K., Kalk, K. H., van Zanten, B. A., Dauter, Z., Kingma, J., Witholt, B., and Hol, W. G. (1993) Refined structure of *Escherichia coli* heat-labile enterotoxin, a close relative of cholera toxin, *J. Mol. Biol. 230*, 890−918.
12. Merritt, E. A., Pronk, S. E., Sixma, T. K., Kalk, K. H., van Zanten, B. A., and Hol, W. G. (1994) Structure of partially activated *E. coli* heat-labile enterotoxin (LT) at 2.6 Å resolution, *FEBS Lett. 337*, 88−92.
13. van den Akker, F., Merritt, E. A., Pizza, M., Domenighini, M., Rappuoli, R., and Hol, W. G. (1995) The Arg7Lys mutant of heat-labile enterotoxin exhibits great flexibility of active site loop 47−56 of the A subunit, *Biochemistry 34*, 10996−11004.
14. Jobling, M. G., and Holmes, R. K. (2001) Biological and biochemical characterization of variant A subunits of cholera toxin constructed by site-directed mutagenesis, *J. Bacteriol. 183*, 4024−4032.
15. Kharadia, S. V., and Graves, D. J. (1987) Relationship of phosphorylation and ADP-ribosylation using a synthetic peptide as a model substrate, *J. Biol. Chem. 262*, 17379−17383.
16. Sigler, P. B., Dryan, M. E., Kiuefer, H. C., and Finkelstein, R. A. (1977) Cholera toxin crystals suitable for X-ray diffraction, *Science 197*, 1277−1279.
17. Otwinowski, Z., and Minor, W. (1997) Processing of X-ray diffraction data collected in oscillation mode, *Methods Enzymol. 276*, 307−326.
18. Vagin, A., and Teplyakov, A. (1997) MOLREP: an automated program for molecular replacement, *J. Appl. Crystallogr. 30*, 1022−1025.
19. CCP4 (1994) The CCP4 (Collaborative Computational Project 4) suite: programs for protein crystallography, *Acta Crystallogr., Sect. D: Biol. Crystallogr. 50*, 760−763.
20. Merritt, E. A., Kuhn, P., Sarfaty, S., Erbe, J. L., Holmes, R. K., and Hol, W. G. (1998) The 1.25 Å resolution refinement of the cholera toxin B-pentamer: evidence of peptide backbone strain at the receptor-binding site, *J. Mol. Biol. 282*, 1043−1059.
21. Murshudov, G. N., Vagin, A. A., and Dodson, E. J. (1997) Refinement of Macromolecular Structures by the Maximum-Likelihood Method, *Acta Crystallogr., Sect. D: Biol. Crystallogr. 53*, 240−255.
22. McRee, D. E. (1999) XtalView/Xfit−A versatile program for manipulating atomic coordinates and electron density, *J. Struct. Biol. 125*, 156−165.
23. Merritt, E. A., Sixma, T. K., Kalk, K. H., van Zanten, B. A., and Hol, W. G. (1994) Galactose-binding site in *Escherichia coli* heat-

labile enterotoxin (LT) and cholera toxin (CT), *Mol. Microbiol. 13*, 745−753.

24. Laskowski, R. A., MacArthur, M. W., Moss, D. S., and Thornton, J. M. (1993) Procheck: a program to check the stereochemical quality of protein structures, *J. Appl. Crystallogr. 26*, 283−291.
25. van den Akker, F., Pizza, M., Rappuoli, R., and Hol, W. G. (1997) Crystal structure of a nontoxic mutant of heat-labile enterotoxin, which is a potent mucosal adjuvant, *Protein Sci. 6*, 2650−2654.
26. van den Akker, F., Steensma, E., and Hol, W. G. (1996) Tumor marker disaccharide D-Gal-beta 1, 3-GalNAc complexed to heat-labile enterotoxin from *Escherichia coli*, *Protein Sci. 5*, 1184−1188.
27. Lencer, W. I., Constable, C., Moe, S., Jobling, M. G., Webb, H. M., Ruston, S., Madara, J. L., Hirst, T. R., and Holmes, R. K. (1995) Targeting of cholera toxin and *Escherichia coli* heat labile toxin in polarized epithelia: role of COOH-terminal KDEL, *J. Cell Biol. 131*, 951−962.
28. Kahn, R. A., Fu, H., and Roy, C. R. (2002) Cellular hijacking: a common strategy for microbial infection, *Trends Biochem. Sci. 27*, 308−314.
29. Weiss, M. S., Blanke, S. R., Collier, R. J., and Eisenberg, D. (1995) Structure of the isolated catalytic domain of diphtheria toxin, *Biochemistry 34*, 773−781.
30. Hazes, B., and Read, R. J. (1997) Accumulating evidence suggests that several AB-toxins subvert the endoplasmic reticulum-associated protein degradation pathway to enter target cells, *Biochemistry 36*, 11051−11054.
31. Rodighiero, C., Tsai, B., Rapoport, T. A., and Lencer, W. I. (2002) Role of ubiquitination in retro-translocation of cholera toxin and escape of cytosolic degradation, *EMBO Rep. 3*, 1222−1227.
32. Schmitz, A., Herrgen, H., Winkeler, A., and Herzog, V. (2000) Cholera toxin is exported from microsomes by the Sec61p complex, *J. Cell Biol. 148*, 1203−1212.
33. Teter, K., Allyn, R. L., Jobling, M. G., and Holmes, R. K. (2002) Transfer of the cholera toxin A1 polypeptide from the endoplasmic reticulum to the cytosol is a rapid process facilitated by the endoplasmic reticulum-associated degradation pathway, *Infect. Immun. 70*, 6166−6171.
34. Tsai, B., Rodighiero, C., Lencer, W. I., and Rapoport, T. A. (2001) Protein disulfide isomerase acts as a redox-dependent chaperone to unfold cholera toxin, *Cell 104*, 937−948.
35. Rodighiero, C., Aman, A. T., Kenny, M. J., Moss, J., Lencer, W. I., and Hirst, T. R. (1999) Structural basis for the differential toxicity of cholera toxin and *Escherichia coli* heat-labile enterotoxin. Construction of hybrid toxins identifies the A2-domain as the determinant of differential toxicity, *J. Biol. Chem. 274*, 3962−3969.
36. Merritt, E. A., and Bacon, D. J. (1997) Raster3D: Photorealistic Molecular Graphics, *Methods Enzymol. 277*, 505−524.
37. Sixma, T. K., Pronk, S. E., Kalk, K. H., van Zanten, B. A., Berghuis, A. M., and Hol, W. G. (1992) Lactose binding to heat-labile enterotoxin revealed by X-ray crystallography, *Nature 355*, 561−564.

BI0360152